

EEMS: Edge-Prompt Enhanced Medical Image Segmentation Based on Learnable Gating Mechanism

Han Xia¹, Quanjun Li¹, Qian Li¹, Zimeng Li^{2*}, Hongbin Ye¹, Yupeng Liu^{3,4}, Haolun Li⁵, and Xuhang Chen^{6*}

¹School of Advanced Manufacturing, Guangdong University of Technology

²School of Electronic and Communication Engineering, Shenzhen Polytechnic University, Shenzhen, China

³Department of Cardiology, Guangdong Provincial People's Hospital (Guangdong Academy of Medical Sciences), Southern Medical University, Guangzhou, China

⁴Guangdong Cardiovascular Institute, Guangdong Provincial People's Hospital, Guangdong Academy of Medical Sciences, Guangzhou, China

⁵College of Automation, Nanjing University of Posts and Telecommunications, Nanjing, China

⁶School of Computer Science and Engineering, Huizhou University, Huizhou, China

Abstract—Medical image segmentation is vital for diagnosis, treatment planning, and disease monitoring but is challenged by complex factors like ambiguous edges and background noise. We introduce EEMS, a new model for segmentation, combining an Edge-Aware Enhancement Unit (EAEU) and a Multi-scale Prompt Generation Unit (MSPGU). EAEU enhances edge perception via multi-frequency feature extraction, accurately defining boundaries. MSPGU integrates high-level semantic and low-level spatial features using a prompt-guided approach, ensuring precise target localization. The Dual-Source Adaptive Gated Fusion Unit (DAGFU) merges edge features from EAEU with semantic features from MSPGU, enhancing segmentation accuracy and robustness. Tests on datasets like ISIC2018 confirm EEMS's superior performance and reliability as a clinical tool.

Index Terms—Medical image segmentation; Edge enhancement; Prompt-guided

I. INTRODUCTION

Medical image segmentation is vital in computer-aided diagnosis and treatment, designed to accurately distinguish anatomical structures or pathological areas from medical images. It is crucial for early disease diagnosis, treatment planning, and assessing treatment effectiveness. However, the challenges posed by low tissue contrast, blurred lesion edges, irregular shapes, and imaging noise make achieving precise, reliable automatic segmentation difficult. Figure 1 illustrates the effect of medical image segmentation.

Recent advancements in deep learning [1]–[6], especially CNNs, have greatly improved medical image segmentation.

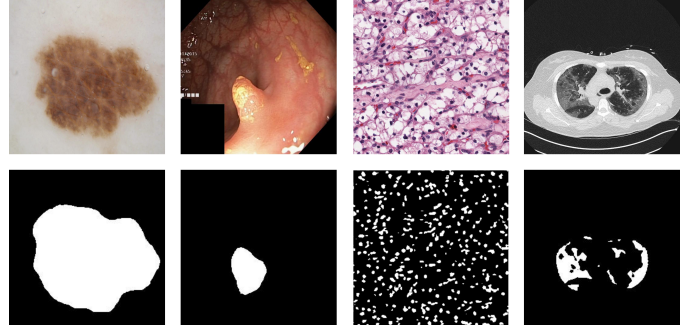


Fig. 1. Effect of segmentation models applied to different body parts

U-Net [7] and its variants, known for their encoder-decoder structure and skip connections, effectively integrate multi-scale features and have become fundamental. However, challenges remain with complex images, particularly in fine edge segmentation and varied lesion shapes. Key issues include capturing multi-frequency information for better edge detail and using high-level semantic information for segmentation guidance.

To address these challenges, this paper proposes EEMS, a novel medical image segmentation model. EEMS's core innovation lies in its dual-branch structure, dedicated to edge enhancement and prompt guidance, with outputs adaptively fused by a Dual-Source Adaptive Gated Fusion Unit (DAGFU). Specifically, EEMS introduces:

- **Edge-Aware Enhancement Unit (EAEU):** This unit significantly enhances edge perception and precise boundary delineation through multi-frequency feature extraction and deformable feature refinement. It integrates multi-scale feature aggregation (with channel attention [8], [9]) and deformable convolution [10] to adaptively process edge information at various frequencies [11], [12].

* Corresponding authors: li_zimeng@szpu.edu.cn, xuhangc@hzu.edu.cn

This work was supported in part by Shenzhen Medical Research Fund (Grant No. A2503006), in part by the National Natural Science Foundation of China (Grant No. 62501412 and 82300277), in part by Shenzhen Polytechnic University Research Fund (Grant No. 6025310023K), in part by Medical Scientific Research Foundation of Guangdong Province (Grant No. B2025610 and B2023012), in part by the National Key Laboratory of Space Intelligent Control (Grant No. HTKJ2025KL502005) and in part by Guangdong Basic and Applied Basic Research Foundation (Grant No. 2024A1515140010).

- **Multi-scale Prompt Generation Unit (MSPGU):** The MSPGU generates and integrates prompt information [13] to guide the model's focus on key regions. It combines local and global context, innovatively employing a multi-scale prompt generation mechanism to produce discriminative prompts for accurate localization and segmentation in complex backgrounds.
- **Dual-Source Adaptive Gated Fusion Unit (DAGFU):** DAGFU adaptively fuses features from EAEU and MSPGU using a learnable gating mechanism [14], rather than simple concatenation. This dynamic strategy intelligently balances edge details and semantic prompts based on image content and task requirements.

Through the synergistic action of EAEU, MSPGU, and DAGFU, the EEMS model comprehensively utilizes image information, significantly improving segmentation accuracy and enhancing robustness to image complexity and noise.

II. METHODOLOGY

A. EEMS Architecture Overview

EEMS adopts a classic encoder-decoder architecture, designed to effectively capture multi-scale and multi-frequency information in medical images. As shown in Fig. 2, the encoder progressively extracts high-level semantic features through a series of downsampling operations, while the EAEU module is responsible for enhancing edge information. The decoder progressively restores spatial resolution through upsampling operations and integrates low-level details by combining skip connections from the encoder. The MSPGU module generates prompt information at each stage, and the Dual-Source Adaptive Gated Fusion Unit (DAGFU) fuses the outputs of the EAEU and MSPGU, ultimately generating a refined segmentation mask.

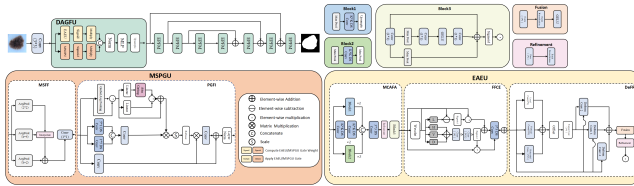


Fig. 2. EEMS Model Architecture Diagram

B. DAGFU: Dual-Source Adaptive Gated Fusion Unit

The Dual-Source Adaptive Gated Fusion Unit (DAGFU) is the core fusion component of EEMS, responsible for effectively fusing the edge-enhanced features generated by EAEU and the prompt-guided features generated by MSPGU. DAGFU is designed with MLP layers and up/downsampling operations to ensure seamless integration of features at different levels. Unlike traditional simple concatenation, DAGFU innovatively introduces a learnable gating mechanism, allowing the model to adaptively control the information flow from EAEU and MSPGU. By learning dynamic gating weights for each branch's features, DAGFU can intelligently decide which

information should be adopted more, thereby achieving finer and more effective feature fusion.

Let F_{EAEU} and F_{MSPGU} be the output features of EAEU and MSPGU, respectively. The gating weights G_{EAEU} and G_{MSPGU} are calculated through 1×1 convolution and Sigmoid activation function:

$$G_{EAEU} = \sigma(\text{Conv}_{1 \times 1}(F_{EAEU})), \quad (1)$$

$$G_{MSPGU} = \sigma(\text{Conv}_{1 \times 1}(F_{MSPGU})). \quad (2)$$

Then, these gating weights are applied to the original features to obtain the gated features F'_{EAEU} and F'_{MSPGU} :

$$F'_{EAEU} = F_{EAEU} \odot G_{EAEU}, \quad (3)$$

$$F'_{MSPGU} = F_{MSPGU} \odot G_{MSPGU}. \quad (4)$$

Finally, the final output of DAGFU, F_{DAGFU_out} , is obtained by concatenating the gated features and passing them through a Multi-Layer Perceptron (MLP) layer for fusion:

$$F_{DAGFU_out} = \text{MLP}(\text{Concat}(F'_{EAEU}, F'_{MSPGU})), \quad (5)$$

where Concat denotes concatenation along the channel dimension, and MLP represents the sequence of 1×1 convolutions and normalization layers used for feature transformation within DAGFU.

C. EAEU: Edge-Aware Enhancement Unit

The Edge-Aware Enhancement Unit (EAEU) aims to significantly enhance the model's perception of image edge details through multi-frequency feature extraction and refinement. The core idea of EAEU is to utilize multi-scale feature aggregation and deformable convolution to adapt to irregular edges. EAEU mainly consists of the following three sub-modules:

1) **FFCE: Frequency Feature Combination and Enhancement:** The Frequency Feature Combination and Enhancement (FFCE) module utilizes wavelet transform to decompose the image into different frequency components, where high-frequency components are rich in edge and texture information. By processing and fusing these multi-frequency components, FFCE can enhance edge features from the frequency domain, providing the model with more comprehensive detailed information. Let X be the input feature of FFCE. Through wavelet transform, we can obtain low-frequency component L and high-frequency components LH, HL, HH . First, the high-frequency components LH, HL, HH are fused through concatenation and a 1×1 convolution Φ_{HF} , yielding the fused high-frequency feature H_{fused} :

$$H_{fused} = \Phi_{HF}(\text{Concat}(\text{Upsample}(LH), \text{Upsample}(HL), \text{Upsample}(HH))), \quad (6)$$

where Upsample denotes the upsampling operation. Next, high-frequency attention feature x_1 and low-frequency difference attention feature x_2 are calculated through the Sigmoid activation function and element-wise multiplication:

$$x_1 = \sigma(\text{Conv}_{1 \times 1}(H_{fused})) \odot X, \quad (7)$$

$$x_2 = \sigma(X - L) \odot X. \quad (8)$$

Then, x_1 and x_2 are concatenated and passed through a fusion module Φ_{Final} to obtain the final fused feature F_{final} :

$$F_{final} = \Phi_{Final}(\text{Concat}(x_1, x_2)), \quad (9)$$

where Φ_{Final} is a fusion module consisting of 1×1 convolution, batch normalization, and GELU activation. Finally, the output of FFCE, F_{FFCE_out} , is obtained by passing F_{final} through a refinement module Refinement and then performing a residual connection with the original input X :

$$F_{FFCE_out} = X + \text{Refinement}(F_{final}). \quad (10)$$

2) *MCAFA: Multi-Scale Channel Attention Feature Aggregation*: The Multi-Scale Channel Attention Feature Aggregation (MCAFA) module utilizes convolutional kernels of different sizes and sampling operations (such as upsampling and max pooling) to capture image features at multiple scales. It enhances the perception of multi-scale edges by processing information from different receptive fields in parallel. To further optimize the aggregation effect of multi-scale features, we innovatively introduced a channel attention mechanism in the MCAFA module. This mechanism can adaptively learn and emphasize the importance of different-scale feature channels, effectively suppressing redundant information, thereby generating more discriminative and informative fused features, greatly enhancing the model's ability to capture fine edge details. Its mathematical representation is as follows:

$$M_c(F) = \sigma(\text{Conv}_{1 \times 1}(\text{ReLU}(\text{Conv}_{1 \times 1}(\text{AvgPool}(F)))) + \text{Conv}_{1 \times 1}(\text{ReLU}(\text{Conv}_{1 \times 1}(\text{MaxPool}(F)))), \quad (11)$$

where F is the input feature map, AvgPool and MaxPool represent global average pooling and global max pooling respectively, $\text{Conv}_{1 \times 1}$ is a 1×1 convolution, ReLU is the activation function, and σ is the Sigmoid activation function. Finally, the channel attention-weighted feature F_{MCAFA_out} is:

$$F_{MCAFA_out} = M_c(F_{extracted}) \odot F_{extracted}, \quad (12)$$

where $F_{extracted}$ is the feature after initial multi-scale feature concatenation and extraction layers in the MCAFA module, and \odot denotes element-wise multiplication.

3) *DeFR: Deformable Feature Refinement*: The Deformable Feature Refinement (DeFR) module is a key component of EAEU, which utilizes deformable convolution to adapt to the geometric deformation of target objects. Unlike traditional convolutions, deformable convolutions learn offsets for each sampling point, allowing the convolutional kernel to adaptively adjust its receptive field, thereby more precisely capturing irregular edges and complex lesion structures. This is particularly important for lesions with varied morphologies in medical images, ensuring the accuracy of edge segmentation. Let F_{in} be the input feature of DeFR. First, the offset Δ_o is generated by the directional offset generator Ψ_{offset} :

$$\Delta_o = \Psi_{offset}(\text{Concat}(O_{3,3}, O_{15,1}, O_{1,15})), \quad (13)$$

where O_{k_x, k_y} are offset features obtained through convolutions with different receptive fields. Then, the input feature F_{in} and offset Δ_o are fed into deformable convolutions DCN^d with different dilation rates. The outputs D_d of all deformable convolutions are concatenated and passed through a fusion layer Φ_{fusion} to obtain the fused deformable feature F_{deform} :

$$F_{deform} = \Phi_{fusion}(\text{Concat}(D_2, D_3, D_4)), \quad (14)$$

where Φ_{fusion} is a fusion module consisting of 1×1 convolution, batch normalization, and GELU activation. Finally, the output of DeFR, F_{DeFR_out} , is obtained by passing F_{deform} through a refinement module Ω and then performing a residual connection with the original input F_{in} :

$$F_{DeFR_out} = F_{in} + \Omega(F_{deform}). \quad (15)$$

D. MSPGU: Multi-scale Prompt Generation Unit

The Multi-scale Prompt Generation Unit (MSPGU) aims to generate and integrate prompt information, enabling the model to more effectively integrate high-level semantic information with low-level spatial features, thereby achieving accurate localization and segmentation of target regions in complex backgrounds. MSPGU combines local and global prompt generation mechanisms, mainly including the following four sub-modules:

1) *MSFF: Multi-Scale Feature Fusion*: MSPGU innovatively introduces the MSFF method, which fuses feature information from different resolutions when generating low-frequency and high-frequency prompts. Specifically, let X be the input feature of MSPGU. Through average pooling operations at different scales, we obtain multi-scale features P_0, P_k :

$$P_0 = \text{AvgPool}_{\text{kernel}=2}(X), \quad (16)$$

$$P_k = \text{AvgPool}_{\text{kernel}=s_k}(X), \quad \forall s_k \in \{2, 4, \dots\}, \quad (17)$$

where s_k is the pooling kernel size defined in `multi_scale_pool`. To fuse these features, we upsample them to a uniform size (e.g., the size of P_0):

$$P'_k = \text{Interpolate}(P_k, \text{size}(P_0)). \quad (18)$$

Then, the multi-scale fused feature F_{MSFF_fused} is obtained by concatenation and 1×1 convolution:

$$F_{MSFF_fused} = \text{Conv}_{1 \times 1}(\text{Concat}(P_0, P'_1, P'_2, \dots)), \quad (19)$$

where F_{MSFF_fused} will serve as input for Low-Frequency Prompt Generation (LPG) and High-Frequency Prompt Generation (HPG).

2) *PGFI: Prompt-Guided Feature Integration*: The PGFI module is the core of MSPGU, which fuses the generated low-frequency prompt P_L , high-frequency prompt P_H , and original pooled feature P_0 to generate the final prompt-guided feature F_{MSPGU_out} through a cross-attention mechanism.

$$Q = P_H, \quad (20)$$

$$K = P_L, \quad (21)$$

$$V = \text{Linear}_O(P_0), \quad (22)$$

where the attention weight $A = \text{Softmax}(QK^T / \sqrt{d_k})$, where d_k is the feature dimension. The final prompt-guided feature F_{MSPGU_out} is calculated as:

$$F_{MSPGU_out} = \text{Upsample}(\text{LayerNorm}(\text{Linear}_P(AV) + V)) \quad (23)$$

Where Linear_O and Linear_P are linear projection layers, LayerNorm is layer normalization, and Upsample is the up-sampling operation.

III. EXPERIMENTS

A. Datasets and Evaluation Metrics

To comprehensively evaluate the EEMS model's effectiveness, we conducted extensive experiments on four public datasets: ISIC2018 [15], Kvasir [16], Monu-Seg [17], and COVID-19 [18]. Comparisons were made against several existing state-of-the-art models.

B. Implementation Details

All models were implemented in PyTorch and trained on a computing platform equipped with NVIDIA 4090 GPUs. **Optimizer:** We utilized the AdamW optimizer with an initial learning rate of 0.001. **Learning Rate Scheduler:** A CosineAnnealingLR scheduler was employed, with $T_{max} = 50$ and $eta_{min} = 0.00001$. **Loss Function:** A BCE-Dice hybrid loss function was used. Its weights were dynamically adjusted during training ($lambda_{start} = 0.7$, $lambda_{end} = 0.3$, $lambda_{decay_epochs} = 100$) to balance pixel-level classification and region overlap optimization. **Training Epochs:** Models were trained for 200 epochs. **Batch Size:** A batch size of 8 was used. **Image Size:** A progressive training strategy was adopted: 100 epochs with 128×128 image size, followed by 100 epochs with 256×256 image size. **Data Augmentation:** Standard data augmentation techniques, including random rotation, random vertical flip, random horizontal flip, and normalization, were applied.

C. Results and Analysis

To comprehensively evaluate the effectiveness of the EEMS model, we assessed its performance on the ISIC2018, Kvasir, Monu-Seg, and COVID-19 datasets, and compared it with several existing state-of-the-art models.

1) *Performance on ISIC2018 Dataset:* Table I presents the detailed quantitative comparison results of the EEMS model with existing SOTA methods on the ISIC2018 dataset.

TABLE I
PERFORMANCE COMPARISON OF EEMS WITH EXISTING SOTA
METHODS ON ISIC2018 DATASET

Metric	U-Net [7]	MALU-Net [19]	UltraLight-VMUNet [20]	EGE-UNet [21]	VPTTA [22]	SAM-Med2D [23]	MLWNet [24]	EMCAD [25]	EEMS (Ours)
mIoU	0.8004	0.7976	0.8110	0.8108	0.7842	0.7283	0.7650	0.8071	0.8498
Dice	0.8955	0.8971	0.8909	0.8956	0.8613	0.8494	0.8997	0.9188	
Accuracy	0.9404	0.9513	0.9549	0.9495	0.9527	0.9514	0.9535	0.9531	0.9652
Specificity	0.9768	0.9738	0.9699	0.9667	0.9662	0.9742	0.9721	0.9750	0.9787
Sensitivity	0.8161	0.8730	0.8907	0.8896	0.9061	0.8738	0.8891	0.8760	0.9160

Table I clearly demonstrates EEMS's superior performance on the ISIC2018 dataset, surpassing current SOTA models across all metrics. EEMS achieved a remarkable mIoU

of **0.8498**, indicating its enhanced capability in accurately identifying target areas through superior overlap. Its Dice coefficient of **0.9188** further confirms robust pixel-level segmentation accuracy, showing a significant lead over EMCAD (0.8997) and generally outperforming other models. EEMS also exhibited a notable advantage in overall accuracy (**0.9652**) and specificity (**0.9787**), with high specificity highlighting its exceptional precision in identifying background pixels, crucial for minimizing false positives. Furthermore, a sensitivity of **0.9160** indicates effective identification of true lesion pixels, reducing false negatives and notably outperforming current SOTA models. Collectively, EEMS strikes an excellent balance between accuracy and sensitivity, reinforced by its strong specificity. Figure 3 presents EEMS's segmentation predictions on representative ISIC2018 images.

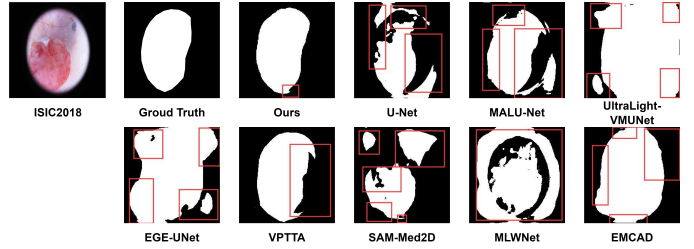


Fig. 3. EEMS Model Visual Segmentation Results

From the visualization results, it can be observed that the EEMS model can generate relatively smooth and accurate segmentation masks, showing good adaptability, especially when dealing with images with blurred lesion boundaries or irregular shapes. These results strongly demonstrate that the EEMS model, through gated feature fusion in the EPMF module, dynamically fuses the output results of EAEU and MSPGU, enabling more comprehensive utilization of image information, improving segmentation accuracy, and enhancing the model's robustness to image complexity and noise, thereby achieving excellent performance in medical image segmentation tasks.

2) *Performance on Kvasir-SEG Dataset:* Table II presents the detailed quantitative comparison results of the EEMS model with existing SOTA methods on the Kvasir-SEG dataset.

TABLE II
PERFORMANCE COMPARISON OF EEMS WITH EXISTING SOTA
METHODS ON KVASIR-SEG DATASET

Metric	U-Net [7]	MALU-Net [19]	UltraLight-VMUNet [20]	EGE-UNet [21]	VPTTA [22]	SAM-Med2D [23]	MLWNet [24]	EMCAD [25]	EEMS (Ours)
mIoU	0.7330	0.5351	0.6100	0.5604	0.5164	0.5911	0.6636	0.7173	0.8121
DSC	0.8459	0.6972	0.7577	0.7182	0.6811	0.7430	0.7977	0.8353	0.8963
Accuracy	0.9253	0.8998	0.9190	0.9108	0.9076	0.9964	0.9076	0.9478	0.9697
Specificity	0.9786	0.9348	0.9441	0.9499	0.9639	0.9964	0.9639	0.9716	0.9811
Sensitivity	0.8145	0.7170	0.7879	0.7068	0.6137	0.6020	0.7620	0.8234	0.9026

On the Kvasir-SEG dataset, EEMS achieved the best performance in mIoU, Dice, and Sensitivity metrics, especially reaching **0.8121** in mIoU, significantly outperforming other comparative methods. This indicates that EEMS has excellent accuracy and robustness in colonoscopy image polyp segmentation tasks.

3) *Performance on Monu-Seg Dataset*: Table III presents the detailed quantitative comparison results of the EEMS model with existing SOTA methods on the Monu-Seg dataset.

TABLE III
PERFORMANCE COMPARISON OF EEMS WITH EXISTING SOTA
METHODS ON MONU-SEG DATASET

Metric	U-Net [7]	MALU-Net [19]	UltraLight-VMUNet [20]	EGE-UNet [21]	VPTTA [22]	SAM-Med2D [23]	MLWNet [24]	EMCAD [25]	EEMS (Ours)
mIoU	0.6784	0.5133	0.5600	0.5009	0.4151	0.2699	0.6535	0.5603	0.6543
DSC	0.5934	0.6784	0.7180	0.6674	0.5867	0.4250	0.7034	0.7182	0.7910
Accuracy	0.9784	0.9444	0.9094	0.8873	0.8662	0.9433	0.9332	0.9263	0.9159
Specificity	0.9640	0.9408	0.9406	0.9386	0.9188	0.9977	0.9540	0.9322	0.9367
Sensitivity	0.8587	0.7248	0.7489	0.7351	0.5911	0.2774	0.8187	0.7461	0.8187

On the Monu-Seg dataset, EEMS performed excellently in mIoU, Dice, and Sensitivity metrics, especially reaching **0.8187** in Sensitivity, indicating its strong ability to identify cell nuclei. Although slightly lower than U-Net in mIoU and Dice, its various metrics are at the upper level among current SOTA models, demonstrating its outstanding performance in nucleus segmentation tasks.

4) *Performance on COVID-19 Dataset*: Table IV presents the detailed quantitative comparison results of the EEMS model with existing SOTA methods on the COVID-19 dataset.

TABLE IV
PERFORMANCE COMPARISON OF EEMS WITH EXISTING SOTA
METHODS ON COVID-19 DATASET

Metric	U-Net [7]	MALU-Net [19]	UltraLight-VMUNet [20]	EGE-UNet [21]	VPTTA [22]	SAM-Med2D [23]	MLWNet [24]	EMCAD [25]	EEMS (Ours)
mIoU	0.3605	0.4811	0.5532	0.3912	0.4591	0.4025	0.4295	0.4120	0.7073
DSC	0.5300	0.6497	0.7123	0.5624	0.6293	0.5739	0.6009	0.5835	0.8286
Accuracy	0.9784	0.9845	0.9867	0.9805	0.9859	0.9856	0.9848	0.9790	0.9915
Specificity	0.9881	0.9932	0.9933	0.9909	0.9968	0.9981	0.9872	0.9966	0.9941
Sensitivity	0.5488	0.6176	0.7092	0.5397	0.5203	0.4359	0.6221	0.6334	0.8808

On the COVID-19 dataset, EEMS achieved the best performance in mIoU, DSC, Accuracy, and Sensitivity metrics. Its performance in mIoU, DSC, and Sensitivity reached **0.7073**, **0.8286**, and **0.8808** respectively, which are significantly ahead of current SOTA models. This indicates that EEMS has powerful capabilities in lung lesion segmentation tasks and can effectively process complex CT images.

D. Ablation Studies

1) *Analysis of Module Effectiveness*: To validate the effectiveness of each proposed module within the EEMS model and their respective contributions to overall performance, we conducted a series of ablation experiments. Ablation studies systematically evaluate the importance of each component by observing changes in model performance after removing specific components or sub-modules.

In this study, our primary focus is on the contributions of EAEU, MSPGU, and DAGFU, as well as their key internal sub-modules. Specifically, we assessed their impact by removing the following components:

- EAEU Component Ablation**: Separately removing the MCAFA, FFCE, and DeFR modules.
- MSPGU Component Ablation**: Separately removing the MSFF and PGFI modules.
- DAGFU Component Ablation**: Removing the learnable gating mechanism in DAGFU, which is responsible for

adaptively fusing features from both the EAEU and MSPGU branches.

After each removal, we re-trained and re-evaluated the model on the ISIC2018 dataset, recording changes in various performance metrics. These experiments aim to quantify the specific contribution of each innovative aspect to the model's final segmentation accuracy and robustness.

Figure 4 visually presents the results of these ablation experiments, clearly illustrating the critical role each module plays in enhancing the performance of the EEMS model.

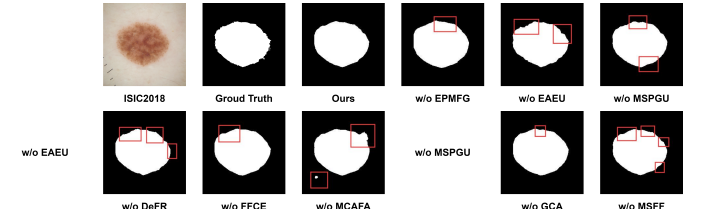


Fig. 4. Ablation experiment results of EEMS on ISIC2018 dataset

2) *Ablation experiment of learnable gating mechanism in the DAGFU*: To verify the effectiveness of the learnable gating mechanism, we conducted an ablation study where we removed it from the DAGFU module and instead used simple feature concatenation for fusion. Table V shows the performance changes of the model on the ISIC2018 dataset after removing the learnable gating mechanism.

TABLE V
LEARNABLE GATING MECHANISM IN DAGFU ABLATION STUDY

Model Configuration	mIoU	Dice	Accuracy
EEMS(Origin)	0.8498	0.9188	0.9656
EEMS (w/o learnable gating mechanism)	0.8212	0.9018	0.9587

As shown in Table V, when the learnable gating mechanism is removed, the model's performance decreased notably, with mIoU dropping from **0.8304** to **0.8250** and Dice from **0.9074** to **0.9020**. This strongly proves the important role of the learnable gating mechanism in DAGFU in adaptively controlling and optimizing the fusion process of edge-enhanced features and prompt-guided features. It can dynamically adjust the information flow according to feature discriminability and task requirements, thereby achieving finer and more effective feature integration, and further improving overall segmentation performance.

3) *Ablation experiment of EAEU and MSPGU*: To deeply analyze the contribution of EAEU and MSPGU, both individually and synergistically, to model performance, we conducted detailed ablation experiments. We compared model configurations using only EAEU, only MSPGU, and both EAEU and MSPGU simultaneously. Table VI shows the performance of these configurations on the ISIC2018 dataset.

From Table VI, it can be seen that when both EAEU and MSPGU are used simultaneously, the model achieved the best performance across all metrics. This indicates that the

TABLE VI
EAEU AND MSPGU EFFECTIVENESS ABLATION STUDY BASED ON ISIC2018 DATASET

Model Configuration	mIoU	Dice	Accuracy
EAEU Only	0.8176	0.8996	0.9569
MSPGU Only	0.8262	0.9048	0.9595
EEMS (EAEU + MSPGU)	0.8498	0.9188	0.9656

synergistic effect of EAEU focusing on edge enhancement and MSPGU focusing on prompt guidance can significantly improve the model's overall segmentation capability.

4) *Ablation experiment of EAEU and MSPGU Sub-modules:* By conducting an ablation study on the effectiveness of each internal component of EAEU and MSPGU, we can quantify the importance of each sub-module. Table VII shows the performance changes of the model on ISIC2018 after removing specific components.

TABLE VII
EAEU AND MSPGU INTERNAL COMPONENT EFFECTIVENESS ABLATION STUDY (BASED ON ISIC2018 DATASET)

Model Configuration	mIoU	Dice	Accuracy
EEMS(Origin)	0.8498	0.9188	0.9656
<i>MSPGU Component Ablation</i>			
w/o MSFF	0.8327	0.9087	0.9618
w/o PGFI	0.8331	0.9089	0.9608
<i>EAEU Component Ablation</i>			
w/o MCAFA	0.8422	0.9143	0.9629
w/o FFCE	0.8316	0.9080	0.9594
w/o DeFR	0.8372	0.9113	0.9618

As shown in Table VII, removing any single component leads to a decrease in model performance, indicating that each sub-module within EAEU and MSPGU is crucial. In particular, the most significant drop in mIoU occurred when PGFI was removed, emphasizing the core role of the PGFI mechanism in integrating multi-source information and improving segmentation accuracy.

IV. CONCLUSION

This paper presents EEMS, a novel model for medical image segmentation, combining the Edge-Aware Enhancement Unit (EAEU) and Multi-scale Prompt Generation Unit (MSPGU). EAEU improves edge perception through multi-frequency feature refinement, while MSPGU enhances high-level semantic integration using a prompt-guided mechanism. Key innovations include channel attention in MCAFA, gated fusion in DAGFU, and multi-scale prompt generation in MSPGU, leading to notable performance gains. Validated on ISIC2018, Kvasir, Monu-Seg, and COVID-19 datasets, EEMS excels in complex edge and target region segmentation. Future work will optimize EAEU, MSPGU, explore advanced fusion strategies, and test EEMS's generalization on varied datasets.

REFERENCES

- [1] H. Li, F. Zheng, Y. Liu, J. Xiong, W. Zhang, H. Hu, and H. Gao, "Adaptive skeleton prompt tuning for cross-dataset 3d human pose estimation," in *ICASSP*. IEEE, 2025, pp. 1–5.
- [2] H. Li and C.-M. Pun, "Monocular robust 3d human localization by global and body-parts depth awareness," *TCSVT*, vol. 32, no. 11, pp. 7692–7705, 2022.
- [3] W. Liu, X. Cun, and C.-M. Pun, "Dh-gan: Image manipulation localization via a dual homology-aware generative adversarial network," *PR*, p. 110658, 2024.
- [4] W. Liu, X. Cun, C.-M. Pun, M. Xia, Y. Zhang, and J. Wang, "Coordfill: Efficient high-resolution image inpainting via parameterized coordinate querying," in *AAAI*, vol. 37, no. 2, 2023, pp. 1746–1754.
- [5] H. Li and C.-M. Pun, "Cee-net: complementary end-to-end network for 3d human pose generation and estimation," in *AAAI*, vol. 37, no. 1, 2023, pp. 1305–1313.
- [6] W. Liu, X. Shen, H. Li, X. Bi, B. Liu, C.-M. Pun, and X. Cun, "Depth-aware test-time training for zero-shot video object segmentation," in *CVPR*, 2024, pp. 19218–19227.
- [7] O. Ronneberger, P. Fischer, and T. Brox, "U-net: Convolutional networks for biomedical image segmentation," in *MICCAI*, 2015, pp. 234–241.
- [8] J. Hu, L. Shen, and G. Sun, "Squeeze-and-excitation networks," in *CVPR*, 2018, pp. 7132–7141.
- [9] S. Woo, J. Park, J.-Y. Lee, and I. S. Kweon, "Cbam: Convolutional block attention module," in *ECCV*, 2018, pp. 3–19.
- [10] J. Dai, H. Qi, Y. Xiong, Y. Li, G. Zhang, H. Hu, and Y. Wei, "Deformable convolutional networks," in *ICCV*, 2017, pp. 764–773.
- [11] J. H. Nam and et al., "Modality-agnostic domain generalizable medical image segmentation by multi-frequency in multi-scale attention," in *CVPR*, 2024, pp. 11480–11491.
- [12] W. Liu, X. Shen, C.-M. Pun, and X. Cun, "Explicit visual prompting for low-level structure segmentations," in *CVPR*, 2023, pp. 19434–19445.
- [13] Y. Lei, J. Li, Z. Li, Y. Cao, and H. Shan, "Prompt learning in computer vision: a survey," *Frontiers of Information Technology & Electronic Engineering*, vol. 25, no. 1, pp. 42–63, 2024.
- [14] J. E. A. Ovalle, T. Solorio, M. Montes-y-Gómez, and F. A. González, "Gated multimodal units for information fusion," in *ICLR*, 2017.
- [15] N. C. F. Codella, D. Gutman, M. E. Celebi, B. Helba, M. A. Marchetti, S. W. Dusza, A. Kalloo, K. Liopyris, N. Mishra, H. Kittler, and A. Halpern, "Skin lesion analysis toward melanoma detection: A challenge at the 2017 international symposium on biomedical imaging (isbi), hosted by the international skin imaging collaboration (isic)," in *ISBI*, 2018, pp. 168–172.
- [16] D. Jha, P. H. Smedsrød, M. A. Riegler, P. Halvorsen, T. De Lange, D. Johansen, and H. D. Johansen, "Kvasir-seg: A segmented polyp dataset," in *MMM*, 2019, pp. 451–462.
- [17] T. L. Dinh, S.-G. Kwon, and et al., "Breast tumor cell nuclei segmentation in histopathology images using efficientunet++ and multi-organ transfer learning," *Journal of Korea Multimedia Society*, vol. 24, no. 8, pp. 1000–1011, 2021.
- [18] E. Dong, H. Du, and L. Gardner, "An interactive web-based dashboard to track covid-19 in real time," *The Lancet infectious diseases*, vol. 20, no. 5, pp. 533–534, 2020.
- [19] J. Ruan, S. Xiang, M. Xie, T. Liu, and Y. Fu, "Malunet: A multi-attention and light-weight unet for skin lesion segmentation," 2022.
- [20] R. Wu, Y. Liu, G. Ning, P. Liang, and Q. Chang, "Ultralight vnn-unet: Parallel vision mamba significantly reduces parameters for skin lesion segmentation," *Patterns*, p. 101298, 2025.
- [21] J. Ruan, M. Xie, J. Gao, T. Liu, and Y. Fu, "Ege-unet: An efficient group enhanced unet for skin lesion segmentation," in *MICCAI*, 2023, pp. 481–490.
- [22] Z. Chen, Y. Pan, Y. Ye, M. Lu, and Y. Xia, "Each test image deserves a specific prompt: Continual test-time adaptation for 2d medical image segmentation," in *CVPR*, 2024, pp. 11184–11193.
- [23] J. Ma, Y. Zhang, and F. He, "Sam-med2d: Segment anything in medical images on 2d data," *arXiv*, 2023.
- [24] X. Gao, T. Qiu, X. Zhang, H. Bai, K. Liu, X. Huang, H. Wei, G. Zhang, and H. Liu, "Efficient multi-scale network with learnable discrete wavelet transform for blind motion deblurring," 2024.
- [25] M. M. Rahman, M. Munir, and R. Marculescu, "Emcad: Efficient multi-scale convolutional attention decoding for medical image segmentation," in *CVPR*, 2024, pp. 11769–11779.